

Ising-like Motility Induced Phase Separation is observed upon modulating intercellular interaction strength

**Gargi Mondal(22N0112), Anurag Abhijit Pendse(200260008),
Pawan Kumar Chaurasia(23M0148)**

Abstract:

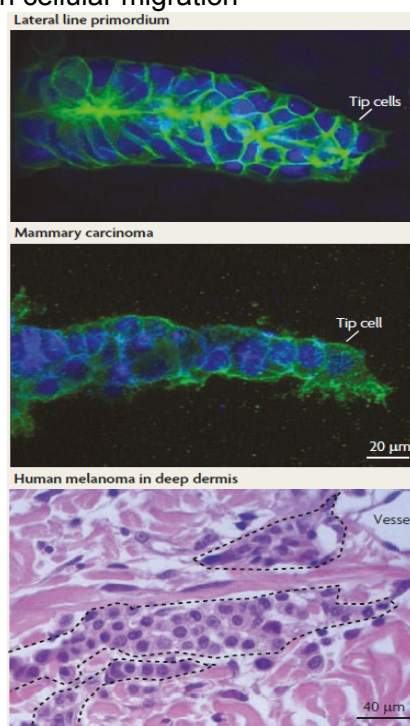
Theoretical lattice models for Contact Inhibition of Locomotion (CIL) show that the system extends an Active Lattice Gas with Ising-like interactions. CIL's broad impact is destabilizing order and, hence, clustering. However, the CIL interaction must compete with the Ising interaction and excluded volume interactions to dictate the system's full dynamics. Including CIL in the Cellular Potts Model (CPM) is possible as both act on similar length and time scales. Both of these show phase transitions with variation in interaction energy. This transition can be observed experimentally to reveal more details regarding the nature of interactions between cells. Microfluidics devices can track the interaction of the circulating tumor cells in the blood vessels using chemokine gradients like glucose.

Background for the theoretical models:

As the interaction Hamiltonian for both the CPM and CIL leads to phase transitions, it is prudent to investigate how much these models match real cells (lung and breast cancer tumor cells). Extensive research has been done on these models through simulations and analytical calculations. Through these simulations and calculations, we have a quantitative picture of the phase transition taking place. The observations can be experimentally verified to provide information about where the model fails. It would allow us to suitably modify the models and provide insight into the physical mechanisms underlying cell migration.

CIL has been shown to play a critical role in cellular collective behavior and it is worthwhile investigating its effects on cellular migration

Figure 1.



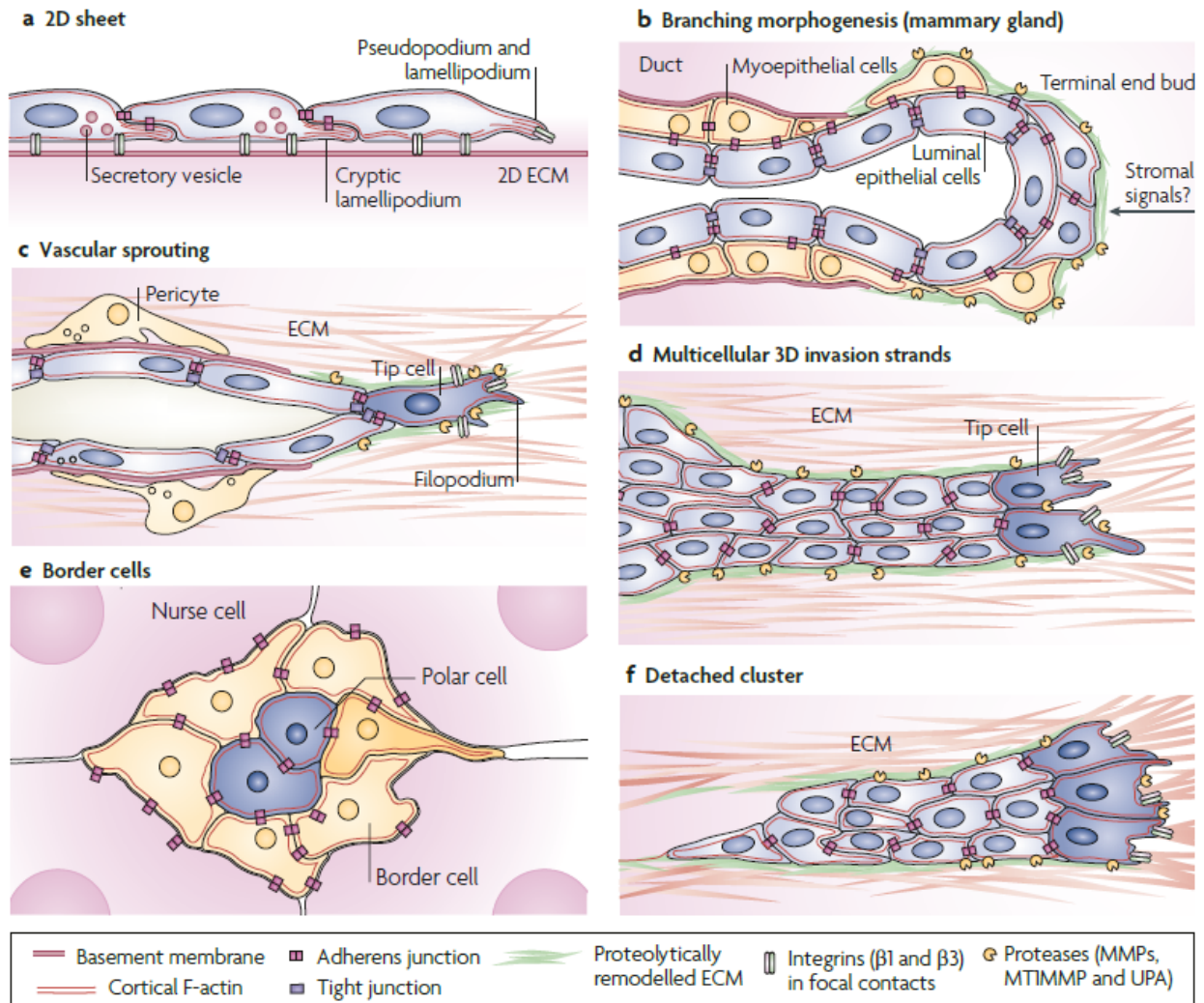
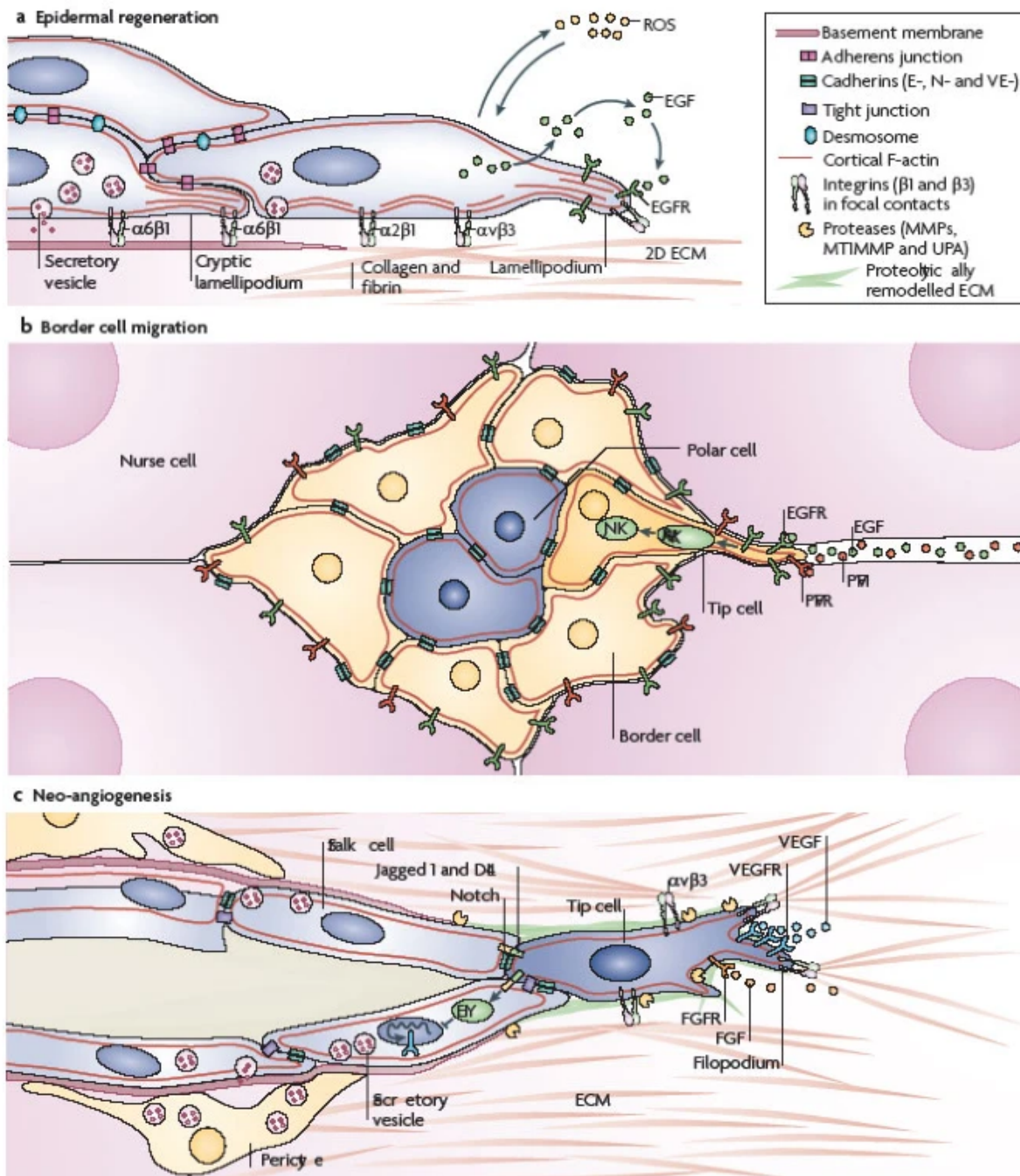


Figure 2: Types and variants of collective cell migration. [2]



Nature Reviews | Molecular Cell Biology

Figure 3: Molecular mechanisms of different forms of collective migration. [2]

Theoretical Modelling:

1) Cellular Potts Model :

The Cellular Potts Model assumes a Hamiltonian of the form [18]

$$H(t) = H_{shape}(t) + H_{adhesion}(t).$$

Here,

$$H_{shape}(t) = H_{volume}(t) + H_{surface}(t) = \sum_{\Sigma_\sigma} \left[\kappa_{\Sigma_\sigma}(t) \left(\frac{v_{\Sigma_\sigma}(t) - V_{\tau(\Sigma_\sigma)}}{v_{\Sigma_\sigma}(t)} \right)^2 + \nu_{\Sigma_\sigma}(t) \left(\frac{s_{\Sigma_\sigma}(t) - S_{\tau(\Sigma_\sigma)}}{s_{\Sigma_\sigma}(t)} \right)^2 \right]$$

$$H_{adhesion}(t) = H_{adhesion}^{int}(t) + H_{adhesion}^{ext}(t) = \sum_{\substack{\mathbf{x} \in \Omega, \mathbf{x}' \in \Omega' \\ \eta(\Sigma_{\sigma(\mathbf{x})}) = \eta(\Sigma_{\sigma(\mathbf{x}')}) \\ \Sigma_{\sigma(\mathbf{x})} \neq \Sigma_{\sigma(\mathbf{x}')}}} J_{\tau(\Sigma_{\sigma(\mathbf{x})}), \tau(\Sigma_{\sigma(\mathbf{x}')})}^{int} + \sum_{\substack{\mathbf{x} \in \Omega, \mathbf{x}' \in \Omega' \\ \eta(\Sigma_{\sigma(\mathbf{x})}) \neq \eta(\Sigma_{\sigma(\mathbf{x}')}) \\ \Sigma_{\sigma(\mathbf{x})} \neq \Sigma_{\sigma(\mathbf{x}')}}} J_{\tau(\Sigma_{\sigma(\mathbf{x})}), \tau(\Sigma_{\sigma(\mathbf{x}')})}^{ext}.$$

Here, the shape of the cell contributes to the energy of the system as well through volume and perimeter constraints (in 2D, volume is equivalent to the area and perimeter is the length of its boundary, while in 3D, volume is the volume of the cell and perimeter is the surface area of the cell). The nature of the geometric constraints is harmonic and enforced through a quadratic energy contribution.

The adhesive energy contributions come from the interaction of the cells with the neighboring filaments (Internal) and the interaction between neighboring cells (External). The model can be evaluated in 2D as well as 3D.

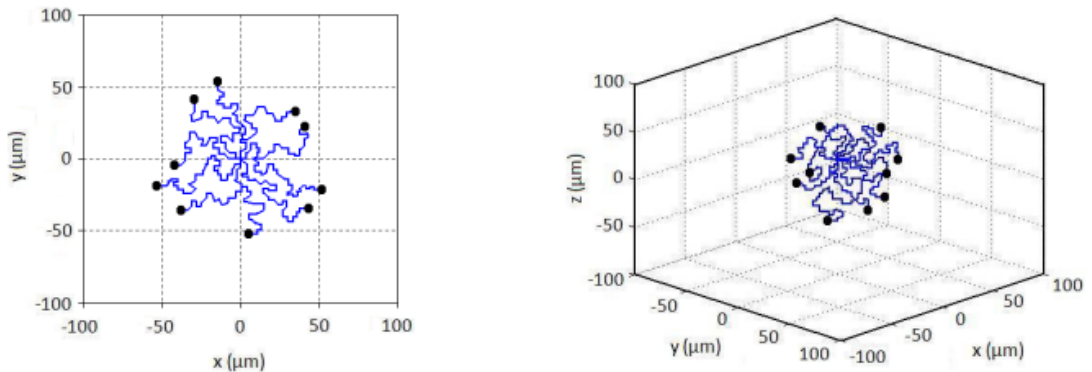


Figure 4: Bottom panels : cell migration on or within the above-represented isotropic ECMS. Wind-rose graphs of 10 randomly chosen cell tracks over 12 h. Black circles represent the ending location of each cell center of mass. [18]

The fiber geometry of the surrounding ECM dictates the motion of the cells very significantly, as is intuitively expected.

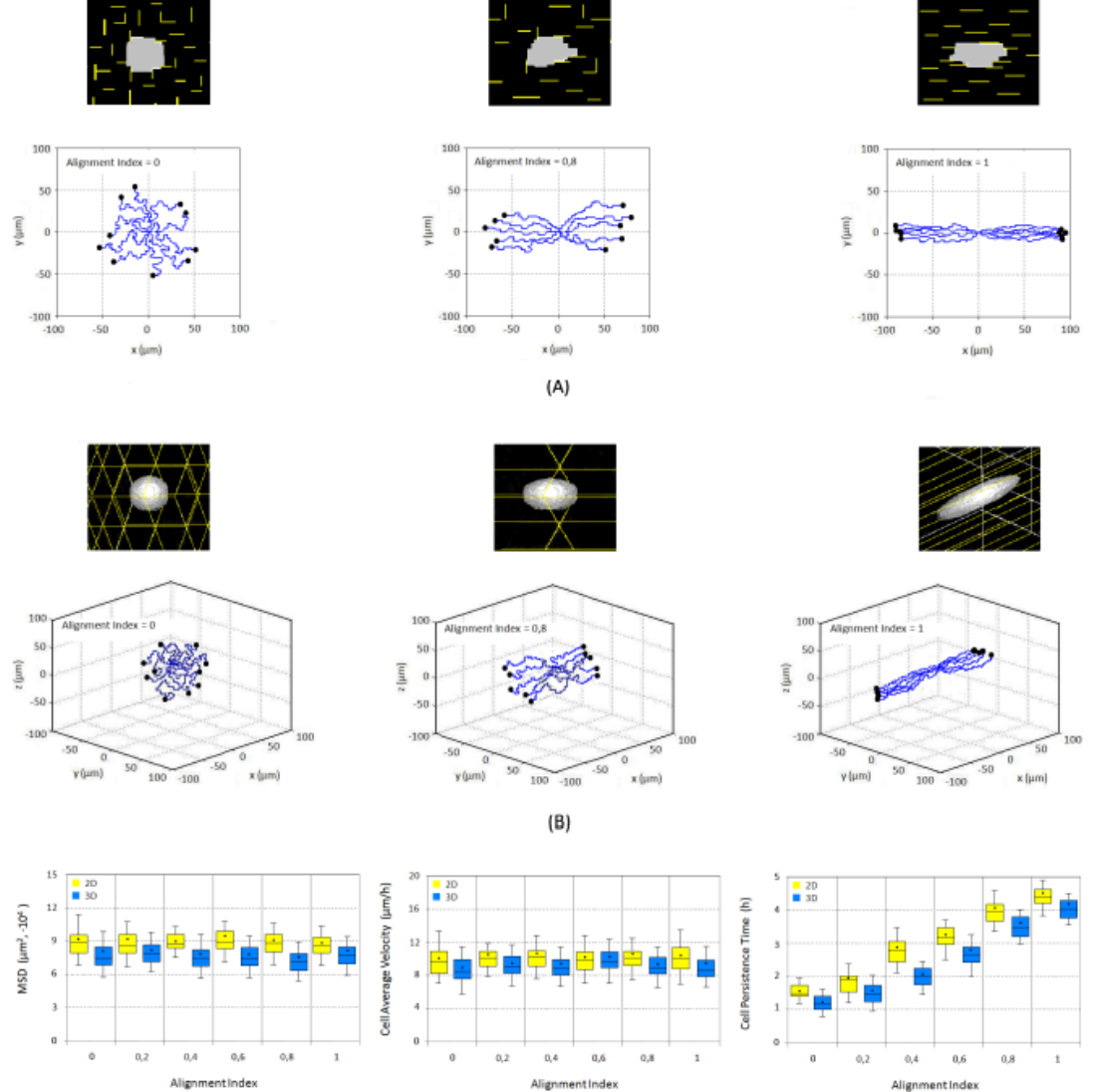


Figure 5: (A, B; top rows) Simulation-obtained cell morphologies. (A, B; bottom rows) Wind-rose graphs of 10 randomly chosen cell tracks over 12 h. (C) Cell mean square displacement (MSD), average velocity and persistence time for both 2D and 3D matrix, displayed with box-and-whisker plots, with box edges as 25th and 75th percentiles and whiskers as 10th and 90th percentiles. [18]

The interaction strengths play a vital role in the migratory aptitudes. As is evident from the plots, we see a non-monotonic dependence of the MSD and cell velocity on the interaction strength between the cell and the surrounding fibers. It is very clear that this is due to competition between intercellular attraction (held constant here) and the

cell-fiber interaction. This non-monotonicity tells us about phase transitions in motility but not about those in EMT. The attraction competes with the motility to give us novel physics.

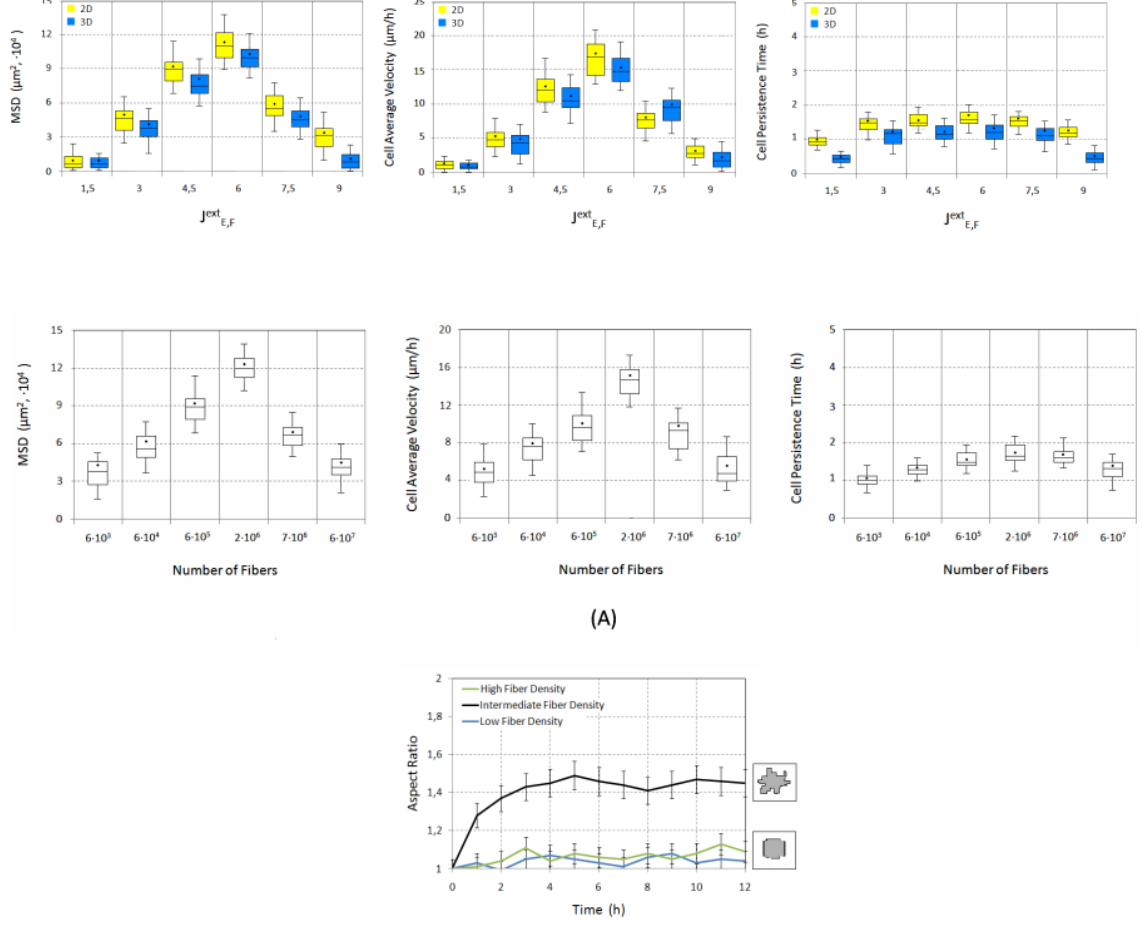


Figure 6: (A) Box-and-whisker plots (means, lines; medians, dots; see appendix) display cell MSD, cell average velocity, and persistence time from 50 randomly selected cells migrating within matrices of decreasing pore size. (B) Cell morphological transitions (evaluated by the cell aspect ratio dened as the ratio between the actual cell surface and the surface of the isovolumic sphere, see appendix) over time upon varying pore dimensions of 20 m (blue line), 10 m (black line), and 5 m (green line). Cell morphologies are obtained from the simulations. Cell elongation increases with decrements of pore size (i.e., increments of ber number) until a threshold value, dened by the limit deformability of the nucleus. As in the following, each value in the plot is shown as mean s.d. over 50 randomly chosen individuals. [18]

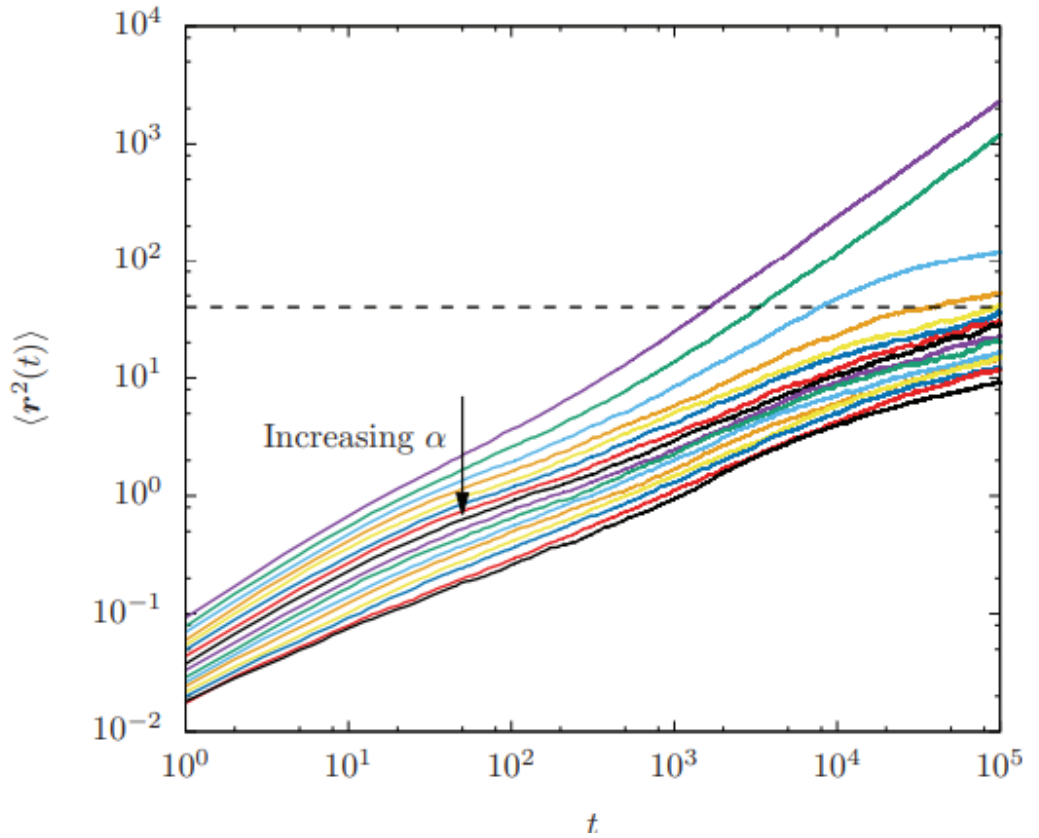
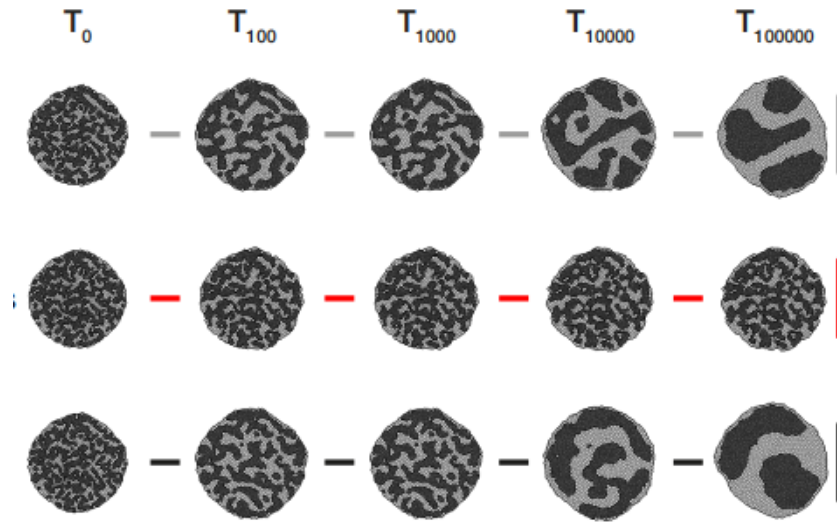


Figure 7: (Colour online) Mean square displacement of the cells vs. time on a log-log plot for $\alpha = 1\text{--}4$ in increments of 0.2 (from top to bottom). The typical intercellular separation (squared) is also plotted as a dashed line to indicate when, on average, the cells have moved from their original position by their size. Notice the difference between the final MSD value for $\alpha = 1.2$ (green curve) and that for $\alpha = 1.4$ (light-blue curve) is more than a decade and is significantly larger than the difference between the final MSD values for higher α . [5]

Here, α is the interaction strength that is being varied at constant motility. [5] We see clustering occur in certain simulations. However, a more controlled set of simulations needs to be conducted to have a better quantitative idea of the cluster size statistics in 2D and 3D.



(<https://doi.org/10.1209/0295-5075/116/28009>)

2) Contact Inhibition of Locomotion:

CIL is a phenomenon that is due to excluded volume and active intercellular forces. We can broadly represent the phenomenon as

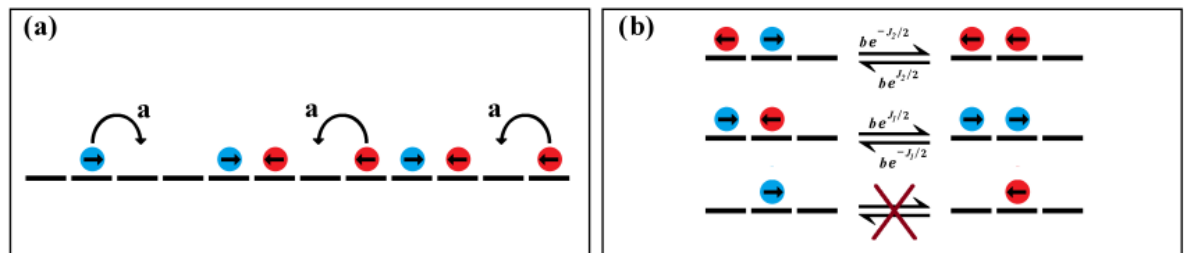


Figure 8: Schematic representation of the relevant dynamical process: (a) Translation process. (b) Polarity switching of a particle at the boundary of a cluster. A single particle bounded by vacancies does not switch its polarity. [19]

The in 1D, Hamiltonian used for the Monte Carlo Simulation can be written as

$$H = \sum_i J_1 \Theta(\sigma_i - \sigma_{i+1}) - J_2 \Theta(\sigma_{i+1} - \sigma_i),$$

Here, σ denotes the velocity of a cell at a site (1,0,-1)[19]
This Hamiltonian can be re-written as

$$H = \sum_i - \left(\frac{J_1 - J_2}{4} \right) \sigma_i \cdot \sigma_{i+1} - \left(\frac{J_1 + J_2}{4} \right) (\sigma_i - \sigma_{i+1}) \cdot \hat{\mathbf{n}}_{i,i+1},$$

This is simply the traditional Ising model with an added (destabilizing) term. Within clusters, we have transition rates as [19]

$$\begin{array}{ccc} \rightarrow \rightarrow \rightarrow & \xrightarrow{\substack{be^{-\Delta J/2} \\ be^{\Delta J/2}}} & \rightarrow \leftarrow \rightarrow \\ \leftarrow \leftarrow \leftarrow & \xrightarrow{\substack{be^{-\Delta J/2} \\ be^{\Delta J/2}}} & \leftarrow \rightarrow \leftarrow \\ \rightarrow \rightarrow \leftarrow & \xrightleftharpoons[b]{b} & \rightarrow \leftarrow \leftarrow \\ \leftarrow \leftarrow \rightarrow & \xrightleftharpoons[b]{b} & \leftarrow \rightarrow \rightarrow \end{array}$$

At the cluster boundaries, we have the rates as [19]

$$\begin{array}{ccc} \rightarrow \rightarrow & \xrightleftharpoons[\substack{be^{-J_2/2} \\ be^{J_2/2}}]{be^{J_2/2}} & \leftarrow \rightarrow \\ \rightarrow \rightarrow & \xrightleftharpoons[\substack{be^{J_1/2} \\ be^{-J_1/2}}]{be^{-J_1/2}} & \rightarrow \leftarrow \\ \leftarrow \leftarrow & \xrightleftharpoons[\substack{be^{-J_2/2} \\ be^{J_2/2}}]{be^{J_2/2}} & \leftarrow \rightarrow \\ \leftarrow \leftarrow & \xrightleftharpoons[\substack{be^{J_1/2} \\ be^{-J_1/2}}]{be^{-J_1/2}} & \rightarrow \leftarrow \end{array}$$

(Let Q be the active Peclet number) we see [19]

The cluster size distribution comes out as [19]

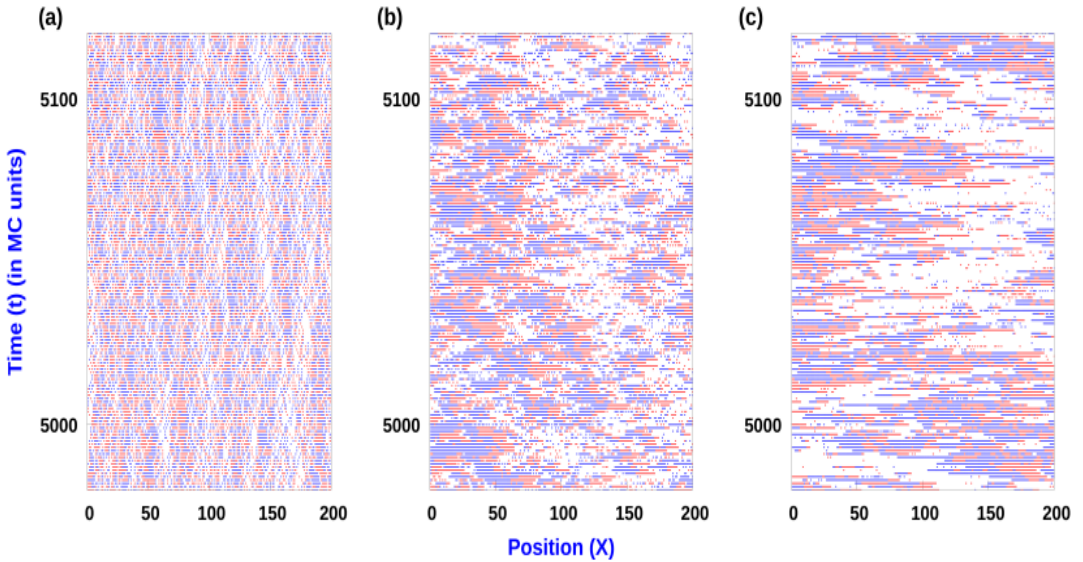


Figure 9: Spatio-temporal plot: Time snapshots of distribution of right polarized (+)(blue) and left polarized (−)(red) particles on the lattice. Here (a) $Q = 0.1$, (b) $Q = 10$, $Q = 50$, $J_1 = 4$, $J_2 = 0$, with $\rho = 0.6$. MC simulations were done with $L = 1000$. [19]

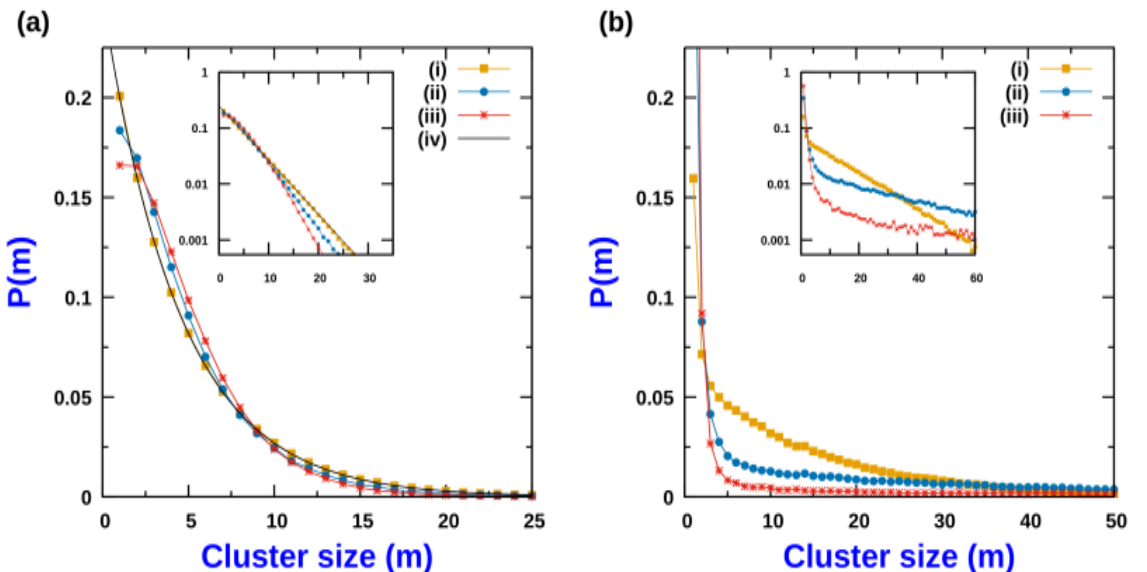


Figure 10: (a) Cluster size (m) probability distribution in the low Q regime; $Q = 0.1$ for different CIL strength: (i) $J_1 = 0.1$, (ii) $J_1 = 3$, (iii) $J_1 = 7$, (iv) Eq.9 (Probability density function for TASEP and SEP). (b) Cluster size (m) probability distribution in the high Q

regime; $Q = 30$ for different CIL strength: (i) $J_1 = 0.1$, (ii) $J_1 = 3$, (iii) $J_1 = 7$. The inset figures are the corresponding logplots. In all cases, $J_2 = 0$, $\rho = 0.8$ and $L = 1000$. MC simulations are performed and averaging is done over 2000 samples. [19]

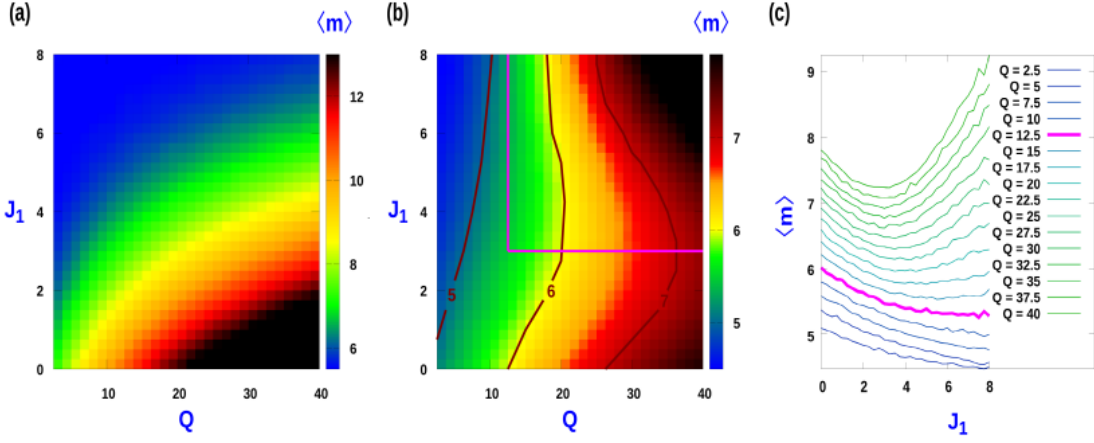


Figure 11: (a) Contour plot of average cluster size $\langle m \rangle$ as function of J_1 and Q when $J_1 = J_2$ i.e. $\Delta J = 0$. (b) Contour plot of average cluster size $\langle m \rangle$ as function of J_1 and Q for constant J_2 ($J_2 = 4$): Re-entrant like behaviour is observed for $Q > Q_c$ with $Q_c = 12.5$. (c) Plot of $\langle m \rangle$ with J_1 corresponding to (b). For all cases, MC simulations where done with $L = 1000$ and averaging was done over 2500 samples at $\rho = 0.8$. [19]

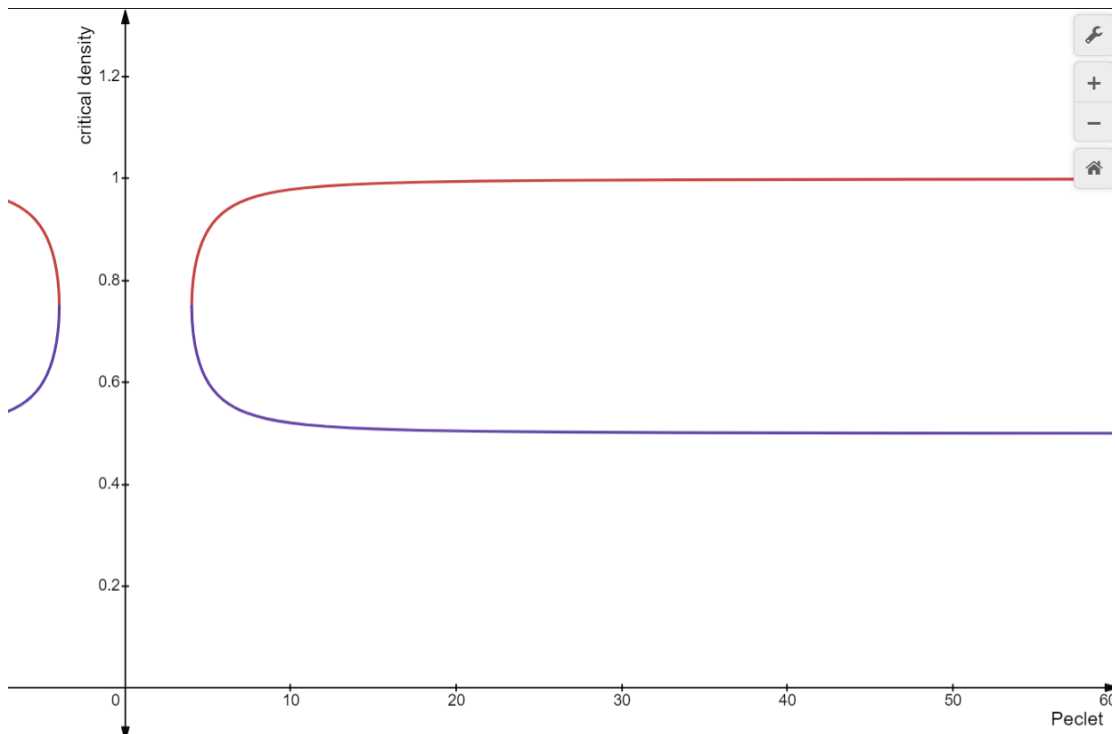
The mean cluster size comes out to [19]

$$\langle m_c \rangle = 1 + \sqrt{1 + \left(\frac{\rho Q - 2}{1 - \rho} \right) e^{J_1/2}}$$

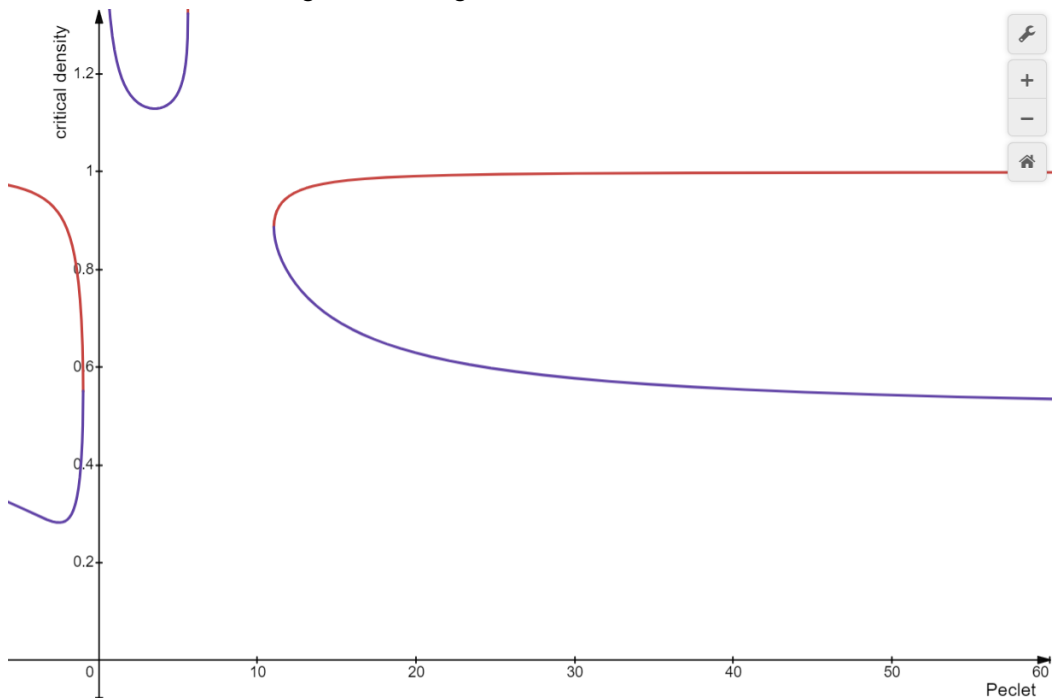
This can be used to fit the experimental data and calculate interaction strengths. We can investigate these expressions analytically as well and obtain the phase transition characteristics using the hydrodynamic equations obtained from the model

$$\begin{aligned} \frac{\partial \rho}{\partial t} &= \frac{\partial^2 \rho}{\partial x^2} - Pe \frac{\partial}{\partial x} (\rho(1 - \rho)) \\ \frac{\partial m}{\partial \tau} &= \frac{\partial^2 m}{\partial x^2} - Pe \frac{\partial}{\partial x} (\rho(1 - \rho)) \\ &\quad + 2 \left(\rho \sinh \left(\beta \Delta J m - \beta J \frac{\partial \rho}{\partial x} \right) - m \cosh \left(\beta \Delta J m - \beta J \frac{\partial \rho}{\partial x} \right) \right) \end{aligned}$$

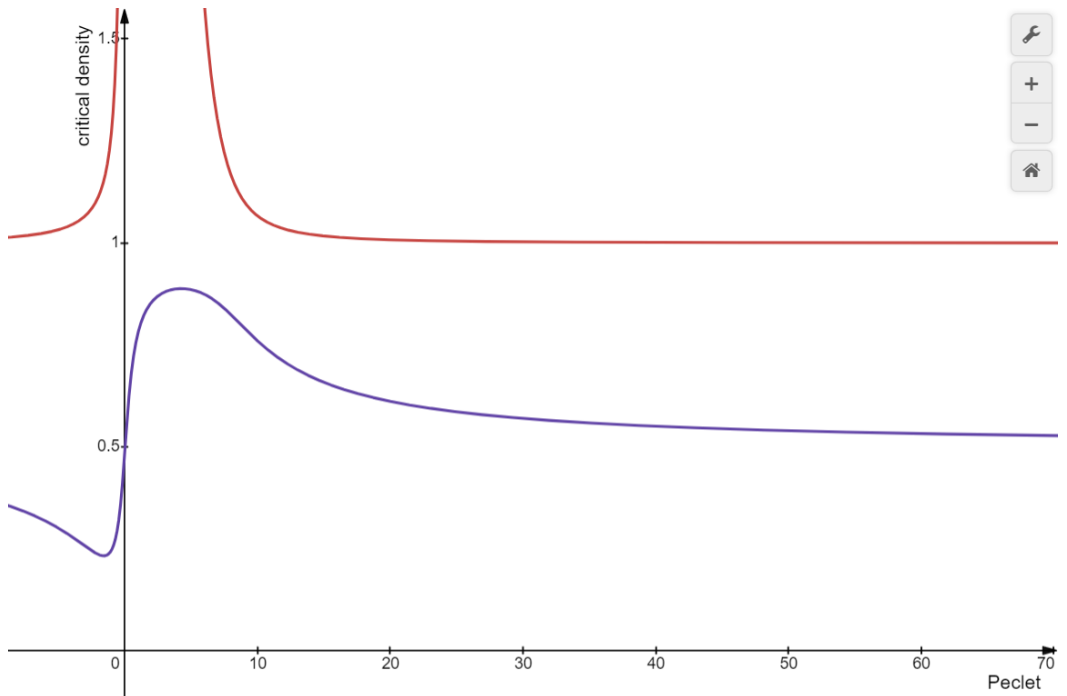
Here, ρ and m are the density and magnetization of the site, respectively. For a fully disordered state, we get



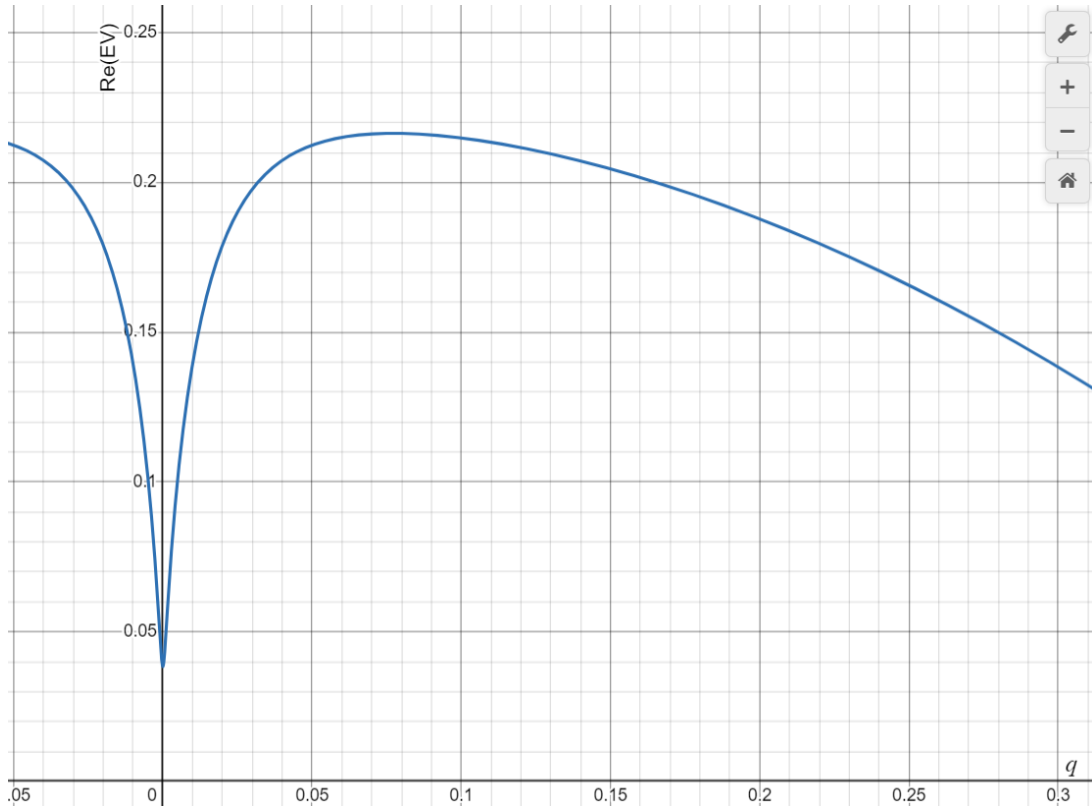
This indicates the instability of the completely disordered state without any interaction. The introduction of CIL gives us a rightward shift as



Moving to higher Ising strength, we get instability at all Peclet numbers.



This indicates that there will be some state with clustering. We can investigate the stability of the fully ordered cluster as



We see system size instabilities occurring in the fully ordered cluster, indicating the formation of smaller clusters.

The distribution of those has been shown through simulations earlier.

3) Curvature of Cell Membranes:

The most prominent candidate whose contribution is overlooked in most migratory models is the membrane curvature. The terms included in the Hamiltonian are volume and perimeter. These account for the bulk modulus of the cell and the young's modulus of the cell membrane. However, as the cell 'flows' through the surrounding matrix, the membrane undergoes curvature changes that will contribute to the dynamics. The cell will move through a competition between the interactions (along with the active motility) with the Ricci flow induced by the curvature changes.

A free energy functional can be defined as

$$\mathcal{H}_{\text{anis}}(C_{\parallel}^0, C_{\perp}^0) = \int dA \left\{ \frac{\kappa_{\parallel}}{2} (C_{\parallel} - C_{\parallel}^0)^2 + \frac{\kappa_{\perp}}{2} (C_{\perp} - C_{\perp}^0)^2 \right\}$$

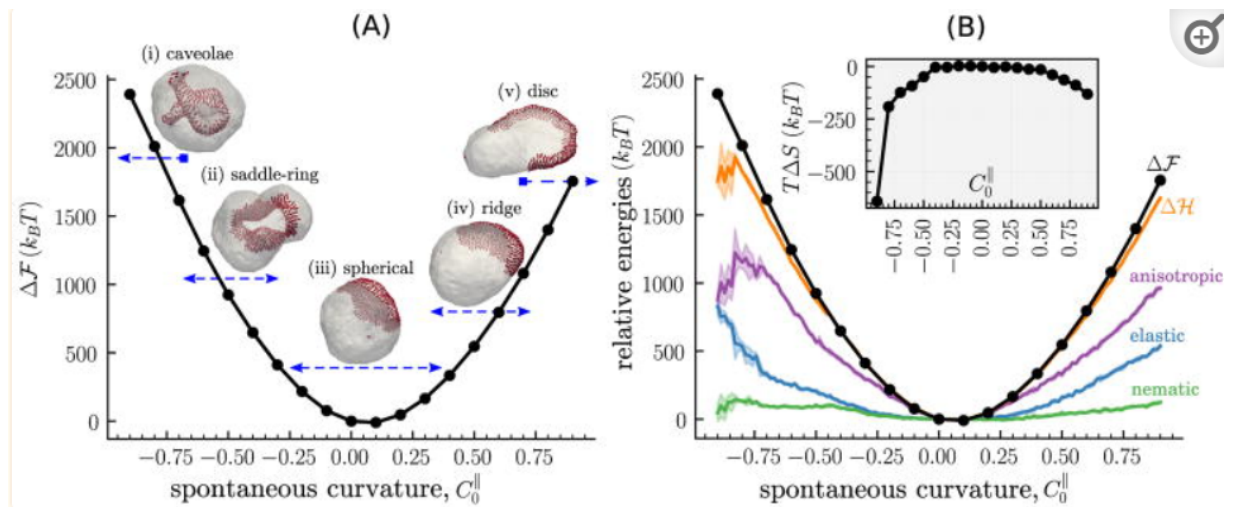


Figure 12. (A) Representative snapshots for nematic membranes with protein concentrations (B) The main panel shows the relative free energies for the five protein concentrations. [4]

Background for Experimental Method:

Epithelial cells are tightly attached with each other by tight junction. But in case of the carcinoma condition this cell-cell attachment get lost due to Epithelial to Mesenchymal Transition (EMT). This EMT transition helps the cell to metastasise. Cancer invasion is a complex phenomenon. It involves different factors like scarcity of nutrients in the tumor bulk, oxygen supply etc. Thus, some of the population of the cancer cells disseminate from the tumor site and get circulating in the blood vessels.[16] This time the cancer cells encounter several challenges like shear stress, immune responses etc. Thus, to survive in that adverse condition

we propose there is some sort of the cell-cell adhesion as well as interaction. This cell-cell adhesion helps them to go to the distant organs.

To prove the interaction levels that we will get from the computational approach, we will check the interaction in the some microfluidics device, where we will mimic the conditions of the blood vessels. Moreover, we will use a chemokine gradients like glucose to observe the cell migration.[17]

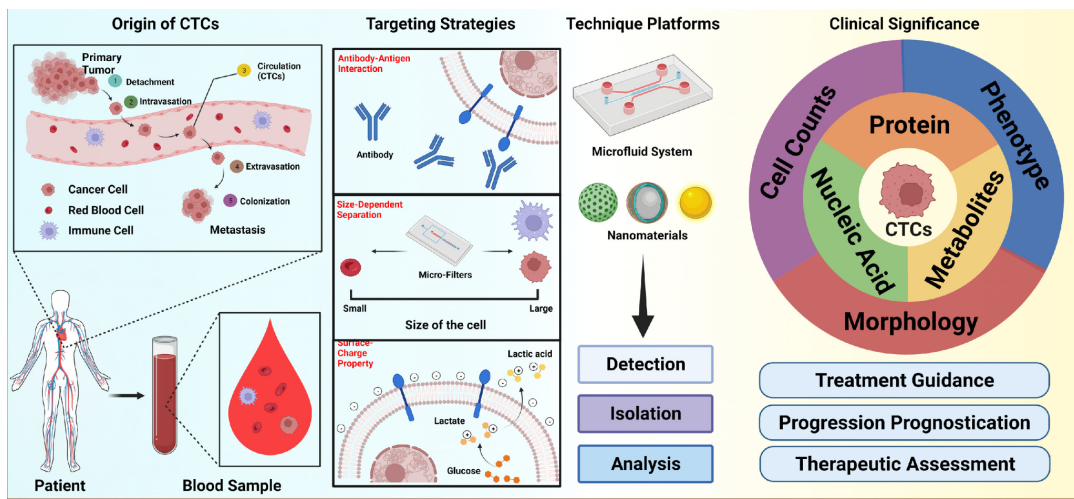


Fig 13: Schematic representation of CTC and its possible detection approach. [16]

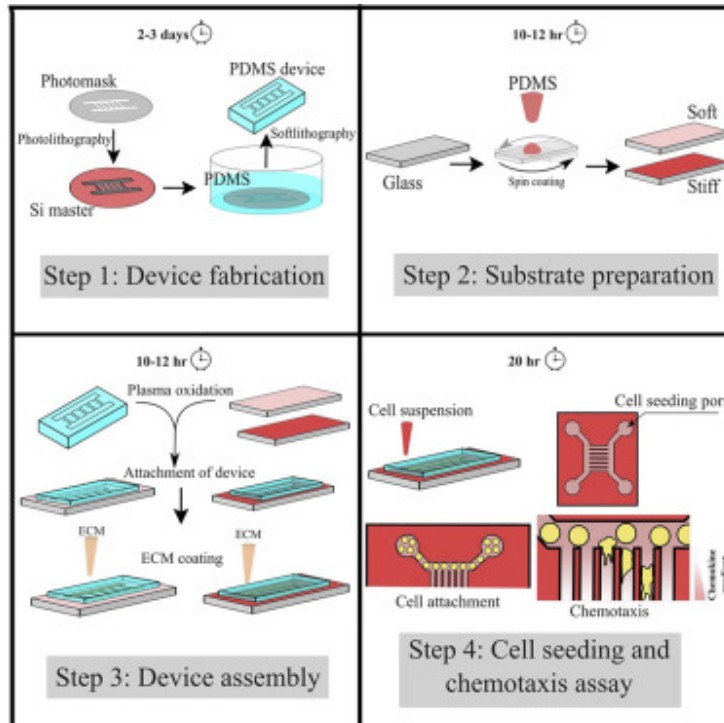


Fig 14: Schematic representation of detection CTC by using microfluidic devices. [17]

Problem Statement: Is there any cluster formation in the circulating tumor cells while migrating in the blood stream?

Objectives:

- 1) To modulate interaction strengths and observe change in collective migratory behavior
- 2) To observe and quantify the kinetics of cluster formation and degradation at the cluster surface
- 3) To probe the cluster size distribution obtained experimentally.

Rationale behind the objectives:

1. Rationale for objective1: The interaction strengths are to be modulated to allow us to observe the behavior of the colony in each case, in particular the EMT score.
2. Rationale for objective2: The cluster size distributions are a direct test of the validity of the underlying model and will reveal the underlying biophysical process.
3. Rationale for objective3: By ex-vivo experiments, the theoretical results will be validated.

Possible Methodology:

1. Computational approach:
 - A. Carrying out simulations to understand the phase diagram of cell-cell interactions in 2D and 3D (Using CIL & CPM based approach).
2. Experimental approach:
 - A. Nature of sample: Blood samples from patient of highly metastatic cancer like lung or breast cancer(Preferably last stage of the cancer).
 - B. Microfluidic devices to isolate circulating cancer cells based on size, using chemokine gradients like glucose.
 - C. To determine the population type and EMT state of the population RNA-seq will be performed.

References:

- 1) Vasudevan, J., Jiang, K., Fernandez, J. G., & Lim, C. T. (2023). Extracellular matrix mechanobiology in cancer cell migration. *Acta biomaterialia*, 163, 351–364.
<https://doi.org/10.1016/j.actbio.2022.10.016>
- 2) Friedl, P., Gilmour, D. Collective cell migration in morphogenesis, regeneration and cancer. *Nat Rev Mol Cell Biol* 10, 445–457 (2009).
<https://doi.org/10.1038/nrm2720>
- 3) Potdar, H., Pagonabarraga, I. & Muhuri, S. Effect of contact inhibition locomotion on confined cellular organization. *Sci Rep* 13, 21391 (2023).
<https://doi.org/10.1038/s41598-023-47986-w>
- 4) Ramakrishnan, N., Bradley, R. P., Tourdot, R. W., & Radhakrishnan, R. (2018). Biophysics of membrane curvature remodeling at molecular and mesoscopic lengthscales. *Journal of physics. Condensed matter : an Institute of Physics journal*, 30(27), 273001.
<https://doi.org/10.1088/1361-648X/aac702>
- 5) Glass transitions in the cellular Potts model, M. Chiang and D. Marenduzzo, *EPL*, 116 2 (2016) 28009
<https://doi.org/10.1209/0295-5075/116/28009>
- 6) A parallelized cellular Potts model that enables simulations at tissue scale, Shabaz Sultan and Sapna Devi and Scott N. Mueller and Johannes Textor, 2023, 2312.09317, arXiv, q-bio.TO
<https://doi.org/10.48550/arXiv.2312.09317>
- 7) Scianna M, Preziosi L, Wolf K. A Cellular Potts Model simulating cell migration on and in matrix environments. *Math Biosci Eng.* 2013;10(1):235-261.
doi:10.3934/mbe.2013.10.235
- 8) Modeling Active Cell Movement With the Potts Model, Guisoni Nara, Mazzitello Karina I., Diambra Luis, *Frontiers in Physics*, 2018
10.3389/fphy.2018.00061
- 9) Antonny B. Mechanisms of membrane curvature sensing. *Annu Rev Biochem.* 2011;80:101-123. doi:10.1146/annurev-biochem-052809-155121
- 10) Shatkin, G., Yeoman, B., Birmingham, K., Katira, P., & Engler, A. J. (2020). Computational models of migration modes improve our understanding of metastasis. *APL bioengineering*, 4(4), 041505. <https://doi.org/10.1063/5.0023748>
- 11) Has, C., Sivadas, P. & Das, S.L. Insights into Membrane Curvature Sensing and Membrane Remodeling by Intrinsically Disordered Proteins and Protein Regions. *J Membrane Biol* 255, 237–259 (2022). <https://doi.org/10.1007/s00232-022-00237-x>
- 12) Sitarska, E., Almeida, S.D., Beckwith, M.S. *et al.* Sensing their plasma membrane curvature allows migrating cells to circumvent obstacles. *Nat Commun* 14, 5644 (2023).
<https://doi.org/10.1038/s41467-023-41173-1>
- 13) Dittrich, F., Speck, T. & Virnau, P. Critical behavior in active lattice models of motility-induced phase separation. *Eur. Phys. J. E* 44, 53 (2021).
<https://doi.org/10.1140/epje/s10189-021-00058-1>

- 14) Pally D, Pramanik D, Bhat R. An Interplay Between Reaction-Diffusion and Cell-Matrix Adhesion Regulates Multiscale Invasion in Early Breast Carcinomatosis. *Front Physiol.* 2019;10:790. Published 2019 Aug 13. doi:10.3389/fphys.2019.00790
- 15) Ruiz-Arrebola S, Guirado D, Villalobos M, Lallena AM. Evaluation of Classical Mathematical Models of Tumor Growth Using an On-Lattice Agent-Based Monte Carlo Model. *Applied Sciences.* 2021; 11(11):5241. <https://doi.org/10.3390/app11115241>
- 16) Deng, Z., Wu, S., Wang, Y., & Shi, D. (2022). Circulating tumor cell isolation for cancer diagnosis and prognosis. *EBioMedicine*, 83, 104237. <https://doi.org/10.1016/j.ebiom.2022.104237>
- 17) Saxena, N., Jadhav, S., & Sen, S. (2021). Fabrication of a microfluidic device for studying the combinatorial effect of physical and chemical cues on cell migration. *STAR protocols*, 2(1), 100310. <https://doi.org/10.1016/j.xpro.2021.100310>
- 18) Marco Scianna, Luigi Preziosi, Katarina Wolf. A Cellular Potts model simulating cell migration on and in matrix environments[J]. *Mathematical Biosciences and Engineering*, 2013, 10(1): 235-261.<https://doi.org/10.3934/mbe.2013.10.235>
- 19) Harshal Potdar, Ignacio Pagonabarraga, Sudipto Muhuri. Effect of Contact Inhibition Locomotion on confined cellular organization. <https://doi.org/10.48550/arXiv.2305.17936>